SCIENCE CHINA
Information Sciences

• Supplementary File •

A Sensing-Memory-Computing Integrated Optoelectronic Synaptic Device Based on Ag/$PtTe_2$/FTO for Artificial Vision Information Processing

Xin Zhang[1†], Xiaojuan Lian[1†*], Shiyu Li[1], Nan He[1], Chaoyi Ban[1], Junyuan Chen[1], Xiaoyan Liu[1], Dapeng Yan[1], Wen Huang[2,3*], Zhikuang Cai[1*] & Lei Wang[1*]

[1]*College of Integrated Circuit Science and Engineering,Nanjing University of Posts and Telecommunications, Nanjing 210023, China*
[2]*Jiangsu Provincial Engineering Research Center of Low Dimensional Physics and New Energy & School of Science, Nanjing University of Posts and Telecommunications, Nanjing 210023, China*
[3]*State Key Laboratory of Silicon and Advanced Semiconductor Materials, School of Materials Science and Engineering, Zhejiang University, Hangzhou 310027, China*

Appendix A Device Fabrication and Characterization

Appendix A.1 Materials Preparation

Prepare a 40 ml solution of N-methylpyrrolidone (NMP) in a test tube and add 40 mg of $PtTe_2$ powder (Sixcarbon Technology Shenzhen). Place the test tube in an ultrasonic bath and perform liquid-phase exfoliation under ultrasonication to obtain a stable dispersion of $PtTe_2$ nanosheets. FTO glass substrates were ultrasonically cleaned sequentially in deionized water, acetone, and ethanol, each for 15 minutes. They were then dried using a nitrogen stream and subjected to 15 minutes of ultraviolet ozone treatment prior to use. Additionally, nickel oxide material was ultrasonically treated in an ultrasonic cleaner for 15 minutes.

Appendix A.2 Device Fabrication

The dispersion containing $PtTe_2$ nanosheets was drop-casted onto the cleaned FTO glass. Spin coating was performed first at 300 rpm for 5 seconds, followed by 1500 rpm for 30 seconds. The sample was annealed on a hotplate at 100 °C for 2 minutes. This spin-coating and annealing process was repeated three times. Finally, a 100 nm-thick silver (Ag) electrode was deposited on top of the device through a shadow mask via thermal evaporation.

Appendix A.3 Characterization

We systematically investigated the structure and performance of the device, including morphological feature analysis, elemental composition identification, and optical property evaluation. The Raman spectrum of $PtTe_2$ (Figure A1(a)) exhibits characteristic peaks at ∼110 cm^{-1} and ∼155 cm^{-1}, corresponding to the in-plane E_g and out-of-plane A_{1g} vibrational modes, respectively, thereby confirming the 1T structural phase [1]. Complementary X-ray diffraction (XRD) characterization (Figure A1(b)) further validate the crystal structure, showing excellent agreement with the P-3m1 (No. 164) space group. The refined lattice parameters ($a = b = 4.0259$ Å, $c = 5.2209$ Å) match well with standard reference data (JCPDS No. 00-018-0977).
The optical absorption spectrum of $PtTe_2$ (Figure A1(c)) confirms its broadband light-harvesting capability across the visible to near-infrared (Vis-NIR) regions. Featuring relatively high absorbance at 405 nm (∼0.12 a.u.) and 532 nm (∼0.13 a.u.), along with significant absorption at 780 nm (∼0.08 a.u.), the material is well-suited for multi-wavelength optical stimulation. Notably, discernible absorption features persist into the NIR region, further highlighting its broadband optical-harvesting potential. Scanning electron microscopy (SEM) imaging (Figure A1(d)) confirms the layered morphology, showing uniformly distributed nanosheets characteristic of $PtTe_2$.

* Corresponding author (email: xjlian@njupt.edu.cn, wenhuang@njupt.edu.cn, whczk@njupt.edu.cn, leiwang1980@njupt.edu.cn)
† These authors contributed equally to this work.

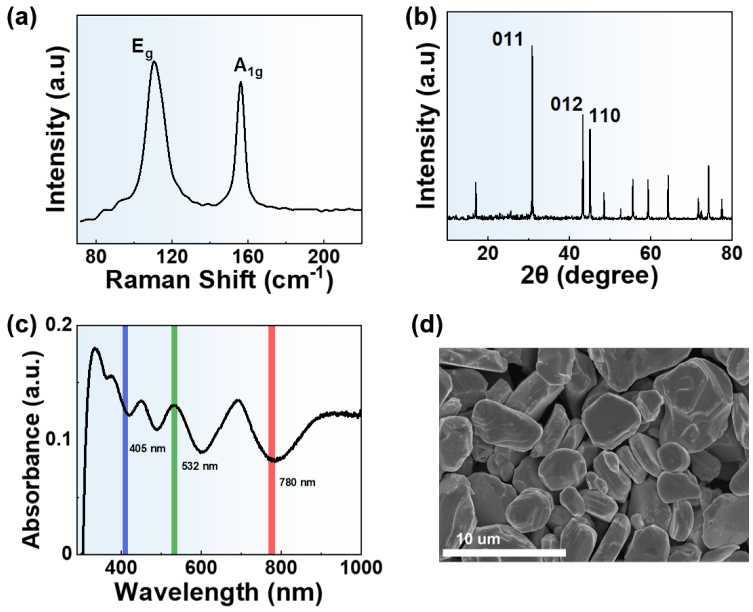

Figure A1 (a) Raman spectra of $PtTe_2$ nanosheets. (b) XRD pattern of the $PtTe_2$ material. (c) Optical absorption spectrum of $PtTe_2$ nanosheets. (d) Surface SEM image of the $PtTe_2$ nanosheets.

Appendix B Electrical and optical characteristics of the device

Figures B1(a–c) characterize the device's robustness, showing stable resistance states and switching voltages over 100 consecutive cycles, alongside multilevel retention exceeding 2×10^3 s. These metrics underscore the device's endurance and stability, which are critical for large-scale AI model implementation. To assess reproducibility, we conducted comprehensive electrical measurements on five independently fabricated devices. As shown in Figure B1(d), all devices exhibit consistent bipolar resistive switching. The statistical distributions of HRS/LRS and Set/Reset voltages [Figures B1(e, f)] reveal minimal device-to-device variation, further validating the uniformity of the fabrication process.

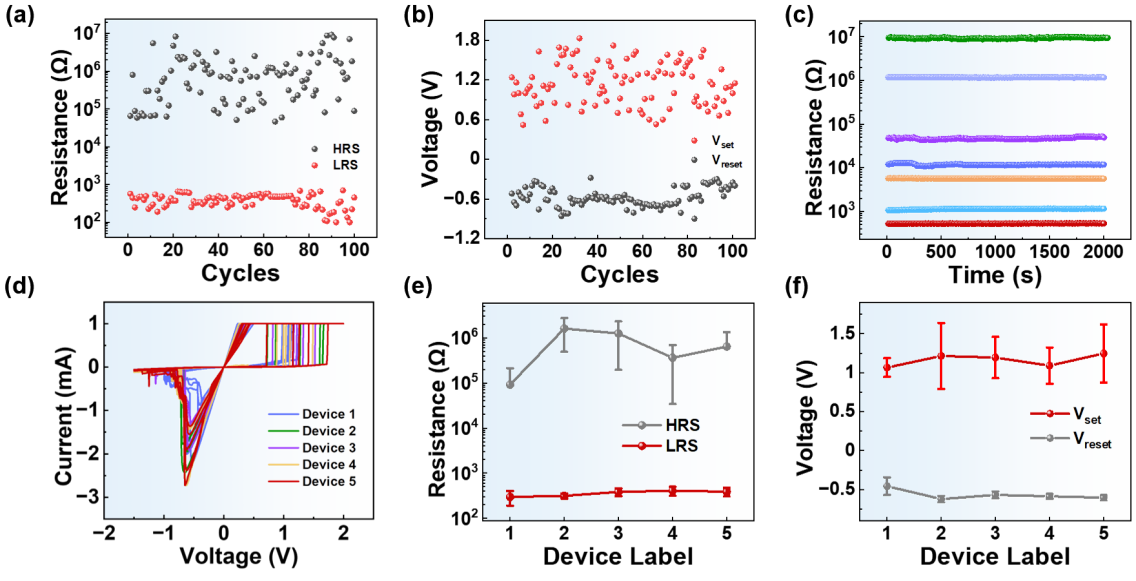

Figure B1 (a) Statistical evolution of HRS and LRS voltages over 100 consecutive DC switching cycles. (b) Statistical evolution of Vset and Vreset over 100 consecutive DC switching cycles. (c) Multilevel resistive state retention, with each state maintained for over 2000 s. (d) I–V curves of five different devices. (e) Resistance error bars for the HRS and LRS of five different devices. (f) Voltage error bars for Vset and Vreset of five different devices.

Figure B2(a) presents the self-powered optical excitatory postsynaptic current (EPSC) under pulse stimulation. The device exhibits

volatile characteristics, spontaneously recovering to its initial synaptic weight without the need for external reset operations. Upon stimulation with 405, 532, and 780 nm optical pulses (5 s duration), the photocurrent decays within 3–5 s and fully returns to baseline within ∼10 s, reflecting the intrinsic volatile timescale of the synaptic response. The variation in photocurrent amplitude is attributed to the wavelength-dependent optical absorption of $PtTe_2$: higher absorbance at 405 and 532 nm enhances the photocarrier generation rate, yielding larger responses, whereas weaker absorption at 780 nm results in a smaller photocurrent.

Figure B2(b) illustrates the synaptic response of the Ag/$PtTe_2$/FTO device under 10 consecutive 532 nm pulses (50 ms width/interval). The highly consistent currents observed over 100 repeated cycles demonstrate exceptional cycling stability and operational reliability. The device also exhibits pronounced spike-width-dependent plasticity (SWDP). As shown in Figure B2(c), increasing the pulse width from 50 ms to 2 s significantly elevates the EPSC from 26 nA to 383 nA. Furthermore, spike-rate-dependent plasticity (SRDP) and spike-power-dependent plasticity (SPDP) are evident. For instance, at pulse frequencies of 10, 6.67, 5, 3.33, and 1.66 Hz, the currents after 20 pulses reach 195, 144, 109, 84, and 50 nA, respectively (Figure B2(d)). Similarly, increasing the optical power density from 0.65 to 2.2 mW/cm^2 (at 0.05 s pulse width) raises the EPSC from 34 nA to 182 nA (Figure B2(e)). These SRDP and SPDP behaviors are consistently confirmed at 405 nm and 780 nm (Figure B2(f–i)), highlighting the device's functional versatility under various optical modulation conditions.

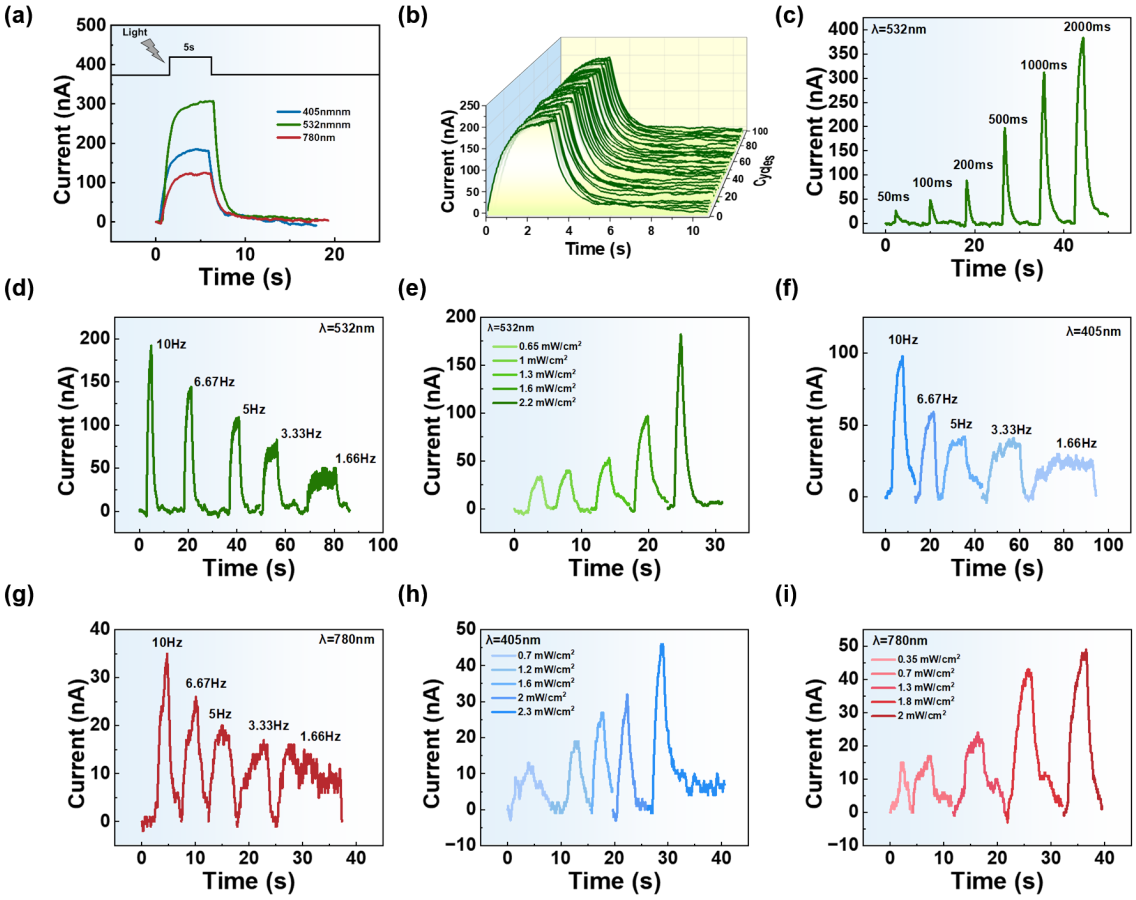

Figure B2 (a) Synaptic currents triggered by optical pulses of different wavelengths with a duration of 5 seconds. (b) Endurance performance over 100 consecutive optical pulses (λ = 532 nm; 10 pulses per train; pulse width: 50 ms; interval: 50 ms). (c) Pulse-width-dependent photocurrent response under 532 nm illumination. Frequency-dependent photocurrent response under (d) 532 nm, (e) 405 nm and (f) 780 nm pulses. Optical power-dependent photocurrent response at (g) 532 nm, (h) 405 nm and (i) 780 nm.

In addition, the device successfully emulates paired-pulse facilitation (PPF). When two consecutive optical pulses (2.2 mW/cm^2, 200 ms) are applied, the second pulse induces a significantly higher current than the first (Figure B3(a), inset). The PPF index is defined as:

$$PPF = \frac{I_2 - I_1}{I_1} \times 100\% \tag{1}$$

where I_1 and I_2 represent the first and second postsynaptic currents, respectively. As shown in Figure B3(a), the PPF index decays from 175% to 12% as the pulse interval increases from 0.05 s to 2 s. The decay curve is fitted by a double-exponential function [2]:

$$\gamma = C_1 \cdot \exp\left(-\frac{t}{\tau_1}\right) + C_2 \cdot \exp\left(-\frac{t}{\tau_2}\right) \tag{2}$$

with time constants $\tau_1 = 76$ ms and $\tau_2 = 573$ ms, corresponding to fast and slow decay components. Physically, these distinct timescales are attributed to the distribution of defect states within the Ag/$PtTe_2$/FTO architecture. The fast relaxation component

(τ_1) corresponds to the rapid detrapping of charge carriers from shallow-level defects, whereas the slow component (τ_2) originates from the sluggish release dynamics of deep-level traps, such as intrinsic Te vacancies in the $PtTe_2$ nanosheets and interfacial states at the FTO junction [3,4]. When the pulse interval is short, carriers trapped in these deep states do not have sufficient time to recombine; the arrival of the second pulse thus triggers a superimposed current response. This mechanism effectively mimics the biological accumulation of neurotransmitters and residual calcium ions, enabling the precise emulation of short-term synaptic plasticity.

Beyond short-term plasticity, the device emulates the learning-forgetting-relearning cycle (Figure B3(b)). While the initial learning phase requires 30 pulses to reach a peak current of 214 nA, the relearning phase—following spontaneous decay to 144 nA—recovers this level with only 15 pulses. This reduced stimulation requirement effectively reproduces the rapid memory recovery characteristic of biological systems. Similarly, the device exhibits robust consistency in its optoelectronic operations. The superimposed photoresponse curves in Figure B3(c) show negligible deviation, while the statistical distributions of response amplitude and decay time in Figures B3(d) and (e) corroborate the high reproducibility of the fabrication process.

We also characterized the optical self-powered performance by measuring the open-circuit voltage (V_{oc}) and short-circuit current (I_{sc}) of the device under different illumination wavelengths (Figure B3(f) and (g)). The V_{oc} values are approximately 0.06 V at 405 nm, 0.11 V at 532 nm, and 0.04 V at 780 nm, with corresponding I_{sc} values of about 176 nA, 268 nA, and 124 nA, respectively. These results further demonstrate the device's intrinsically self-powered photonic operation, enabling photodetection without any external bias. The device exhibits rapid optical dynamics (Figure B3(h)), reaching near-saturation within ∼280 ms and responding distinctively to pulses as short as 20 ms (Figure B3(i)).

By comparing our device with recently reported optoelectronic synaptic devices, we note that the Ag/$PtTe_2$/FTO structure offers a simple architecture, broadband wavelength response, excellent optical self-powered synaptic characteristics, reliable non-volatile electrical switching and high switching ratio (Table B1). In summary, the Ag/$PtTe_2$/FTO device successfully emulates key neurosynaptic functions and complex cognitive behaviors, providing a robust platform for advanced neuromorphic applications.

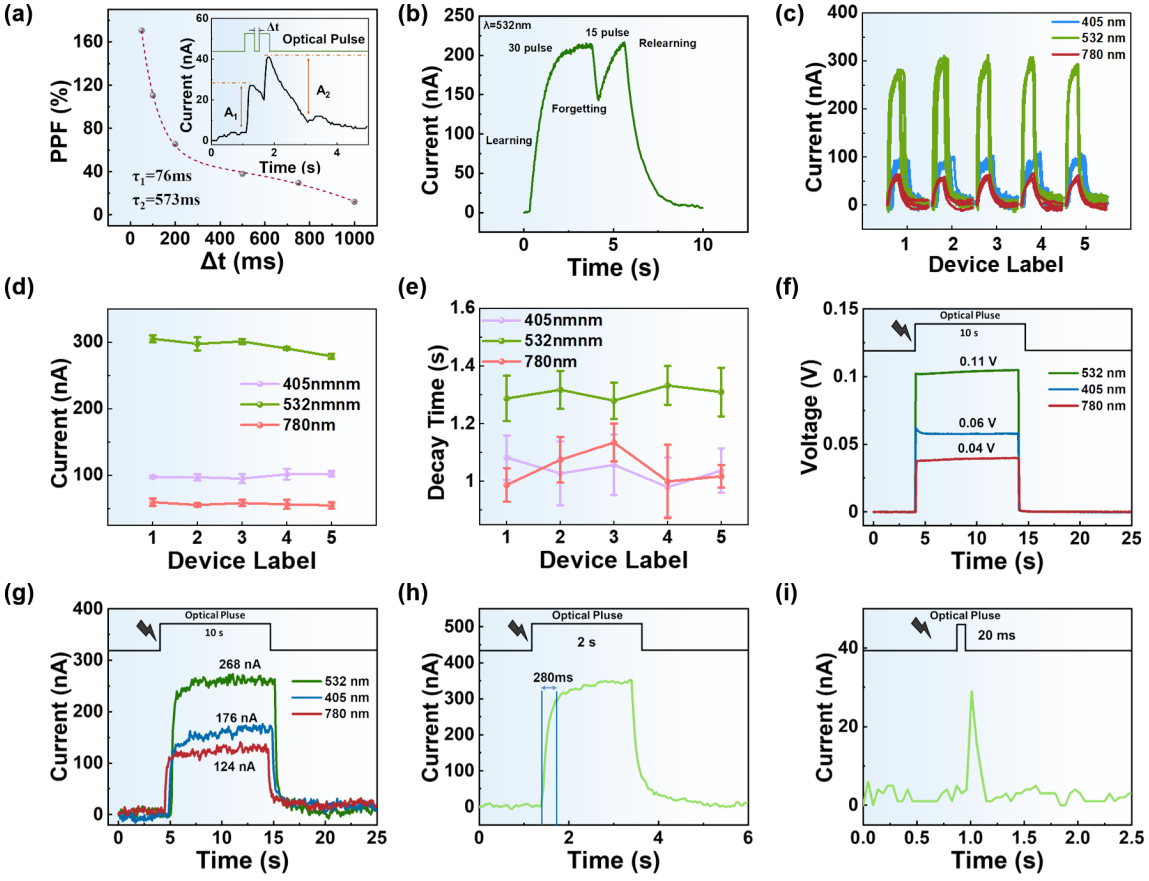

Figure B3 (a) Variation of the paired-pulse facilitation index with inter-pulse interval. (b) Emulation of "learning–forgetting–relearning" behavior using multi-pulse optical stimulation. (c) Optical response curves of five different devices under different wavelengths. (d) Error-bar plot of response current for different devices at different wavelengths. (e) Error-bar plot of decay time for different devices at different wavelengths. (f) Open-circuit voltage (Voc) of the Ag/$PtTe_2$/FTO device under different wavelengths. (g) Short-circuit current (Isc) of the Ag/$PtTe_2$/FTO device under different wavelengths. (h) Switching speed of the Ag/$PtTe_2$/FTO device under a 2 s light pulse, with a turn-on time of approximately 280 ms. (i) Optical response of the Ag/$PtTe_2$/FTO device under a 20 ms light pulse, demonstrating the device's fast response characteristics.

Table B1 Comparison of the performances between different optoelectronic device and our Ag/$PtTe_2$/FTO optoelectronic synaptic device.

Device Structure	λ (nm)	Self-Power	Speed	Ratio	Energy	Endurance	Ref.
Au/Cr/WS_2/SiO_2/Si	435nm,520nm,637nm	√	30ms	-	-	-	[5]
Au/MoS_2/Au	532nm	×	256ms	190	-	-	[6]
Ag/WSe_2/SiO_2/Si	975nm	×	2.5ms	-	-	-	[7]
Au/MoS_2/hBN/Gr/SiO_2/Si	532nm	×	1ms	10^6	40uW	300	[8]
Pt/Ag/ZnO/Pt/Ti	365nm	√	500ms	100	220uW	100	[9]
IL/Au/PM6/Au	465nm,520nm,638nm	√	1s	-	-	-	[10]
PQDs/BP/SiO_2/Si	532nm,635nm,1550nm	×	100ms	-	-	-	[11]
Ag/Ga_2O_3/Pt	365nm,254nm	×	-	10^4	500uW	80	[12]
Ag/BCP/PCBM/$FAPBI_3$/NiO_x/ITO	532nm	√	50ms	-	-	-	[13]
$Mo_xRe_{1-x}S_2$/SiO_2/Si	473nm,532nm,633nm	×	100ms	-	-	-	[14]
Ag/$PtTe_2$/FTO	405, 532, 780	√	20 ms	> 500	90 μW	> 100	This work

Appendix C Work mechanism analysis

The self-powered operation and dynamic photoresponse of the device are fundamentally governed by the interfacial band alignment and carrier transport kinetics. First, the self-powered mechanism arises from the Schottky junction at the FTO/$PtTe_2$ interface. Driven by the work function difference between FTO (∼4.60 eV) and $PtTe_2$ (∼4.29 eV) [15], Fermi-level equilibration induces upward band bending, establishing a built-in electric field [16]. Under illumination, this field efficiently separates photogenerated electron-hole pairs—propelling electrons toward the Ag electrode and holes to the FTO, thereby generating a photocurrent without external bias [17].

Subsequently, the temporal dynamics of this photocurrent are dictated by two competing processes: photocarrier generation and non-equilibrium recombination. Photons excite valence band electrons to the conduction band, while recombination processes relax these carriers back to the ground state via radiative or non-radiative pathways [18]. At the onset of stimulation, high photon-electron conversion efficiency drives an exponential rise in carrier concentration. As carrier density accumulates, the recombination probability increases, eventually balancing the generation rate and leading to photocurrent saturation. This dynamic behavior is quantitatively described by:

$$I(t) = I_0 \left[1 - \exp\left(-\frac{t}{\tau}\right)\right] \tag{3}$$

where I_0 represents the steady-state photocurrent, and τ denotes the carrier transport response time. This model aligns with transient photoconductivity characteristics, confirming that the device's dynamic behavior is shaped by the interplay between carrier generation and recombination within the self-powered architecture.

Appendix D Image Denoising and Classification Tasks

Inspired by the human retina's capability for preliminary sensory preprocessing, this study presents a $PtTe_2$-based optoelectronic synaptic device that integrates image sensing and denoising functionalities to optimize artificial neural visual systems (ANVS). Leveraging the device's highly nonlinear photoresponse, we established a mapping mechanism where high-grayscale features elicit strong excitatory postsynaptic currents (EPSCs), while low-intensity background noise is effectively suppressed, thereby significantly enhancing image contrast without the need for external processing modules (Figure D1(a) and (b)).

To validate this self-denoising capability, KMNIST character images corrupted by Gaussian noise (mean=0.3, variance=0.3) were processed via the device, yielding output images with superior contrast compared to traditional Gaussian and median filtering (Figure D1(c) and d). Subsequent classification using a CNN, with synaptic weights mapped from the device's LTP/LTD characteristics (Figure D1(e) and (f)), achieved a recognition accuracy of 90%. This performance surpasses that of traditional filtering methods and closely approximates noise-free baselines, demonstrating the device's potential as an energy-efficient platform for integrated sensing and in-sensor computing.

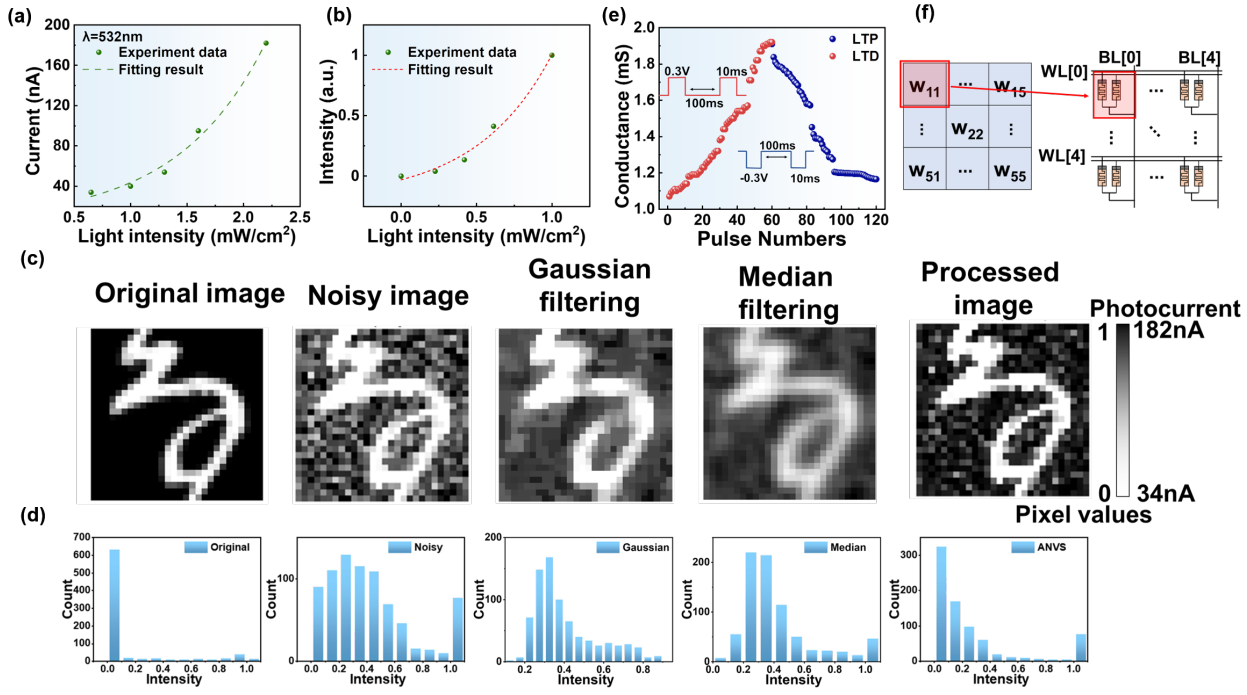

Figure D1 (a) Fitted postsynaptic current (PSC) curves under 532 nm laser illumination at different optical power densities. (b) Fitted correlation between normalized optical power and normalized grayscale intensity. (c) Sample images and their corresponding pixel intensity histograms under original, noisy, and filtered conditions (Gaussian, Median, and ANVS). The noisy image was generated by adding Gaussian noise (mean=0.3, variance=0.3) to the original image, while the denoised images were obtained using the (d) respective filtering algorithms. (e) LTP and LTD characteristics emulated by the proposed electronic synapse of the Ag/$PtTe_2$/FTO optoelectronic synaptic device memristors. (f) Conceptual schematic of conductance-to-weight mapping. The hardware implementation illustrates how device conductance values are mapped to a 5×5 convolutional kernel weight matrix, where "w" denotes an element in the weight matrix, and "G^+" and "G^-" represent the conductance values of devices in a differential pair corresponding to positive and negative weights, respectively.

Appendix E Dynamic Motion Recognition via Spatiotemporal Fusion

To validate the spatiotemporal fusion capabilities enabled by the device's dynamic conductivity, we developed a neuromorphic visual system for monitoring dynamic motion trajectories. In this demonstration, motion videos were recorded at a frame rate of 30 fps, with sequential frames (T_1, T_2, T_3) sampled at intervals of 0.2 s (corresponding to 6 frames). The dataset comprises 400 trajectory samples, generated by repeating vehicle movements 100 times in each of the four cardinal directions, randomly partitioned into a training set (70%) and a testing set (30%).

Leveraging the device's inherent volatility, the system achieved a classification accuracy of 97.5%. In contrast, an ablation study replacing these device dynamics with software-based equal-weighted fusion—under identical network architecture and hyperparameters—yielded only 57.5%, highlighting the critical role of the device's temporal characteristics. Beyond functional performance, the practical viability of this system is underpinned by its excellent scalability and compatibility with standard semiconductor processes. Unlike complex lithography-heavy approaches, our device features a simple two-terminal architecture fabricated via low-cost, solution-based spin-coating. Crucially, this low-temperature processing ensures a minimal thermal budget, making it intrinsically suitable for monolithic Back-End-of-Line (BEOL) integration [19]. This allows the device array to be directly stacked atop pre-processed silicon CMOS logic wafers without inducing thermal damage to underlying circuitry, aligning with emerging breakthroughs in wafer-scale 2D material integration and paving the way for high-density, heterogeneous neuromorphic chips [20].

References

1 Ma H, Chen P, Li B, et al. Thickness-Tunable Synthesis of Ultrathin Type-II Dirac Semimetal $PtTe_2$ Single Crystals and Their Thickness-Dependent Electronic Properties. *Nano Letters*, 2018, 18: 3523-3529.

2 Lian X, Zhang X, Li S, et al. Exploring the potential of 2D $PtTe_2$-based memristors for neuromorphic computing. *Applied Physics Letters*, 2025, 126.

3 Guo H, Wang Y, Li G, et al. Insights into excellent persistent luminescence and detecting trap distribution in $BaHfSi_3O_9:Eu^{2+}$, Pr^{3+}. *Journal of Materials Chemistry C*, 2017, 5: 12090-12096.

4 Wei B, Chen Y, Han X, et al. Ultra-low power MoS_2 optoelectronic synapse with wavelength sensitivity for color target recognition. *Science China Information Sciences*, 2025, 68.

5 Gong Y, Xing X, Wang X, et al. Integrated Bionic Human Retina Process and In-Sensor RC System Based on 2D Retinomorphic Memristor Array. *Advanced Functional Materials*, 2024, 34.

6 Krishnan K N, Sathyanarayana S, Das B C. Grain boundary effect unveiled in monolayer MoS_2 for photonic neuromorphic applications. *Journal of Materials Chemistry C*, 2024, 12: 13827-13839.

7 Lu Y, Chen C, Sun Q, et al. Near-Infrared Synaptic Responses of WSe_2 Artificial Synapse Based on Upconversion Luminescence from Lanthanide Doped Nanoparticles. *Inorganics*, 2025, 13.

8 Yang Q, Luo Z D, Zhang D, et al. Controlled Optoelectronic Response in van der Waals Heterostructures for In-Sensor Computing. *Advanced Functional Materials*, 2022, 32.

9 Wang L, Zhang L, Hua S, et al. In-Sensor Noise Reduction and Reservoir Computing System Using ZnO Optoelectronic Memristors for Artificial Vision Applications. *ACS Applied Electronic Materials*, 2024, 6: 9019-9028.
10 Ge Y, Wang D, Zhou M, et al. An organic optoelectronic synaptic transistor for image preprocessing. *Applied Physics Letters*, 2025, 127.
11 Shao H, Wang W, Zhang Y, et al. Adaptive In-Sensor Computing for Enhanced Feature Perception and Broadband Image Restoration. *Advanced Materials*, 2024, 37.
12 Cui D, Pei M, Lin Z, et al. Versatile optoelectronic memristor based on wide-bandgap Ga_2O_3 for artificial synapses and neuromorphic computing. *Light: Science & Applications*, 2025, 14.
13 Huang W, Tang J, Li B, et al. Design of All-Optical Bidirectional Self-Powered Synaptic Devices for Neuromorphic Computing Applications. *Small*, 2025, 21.
14 Sun X, Wang Z, Si C, et al. $MoxRe(_{1-x})S_2$-Based Optoelectronic Synapse for Artificial Neural Visual System Application. *Advanced Functional Materials*, 2024, 35.
15 Zhang S, Xia Z, Meng J, et al. Electronic and Transport Properties of $InSe/PtTe_2$ van der Waals Heterostructure. *Nano Lett*, 2024, 24: 8402-8409.
16 Liu X, Huang S, Wang K, et al. An Array of Light-Stimulated Two-Terminal Synaptic Devices with the Modulation of Electric Polarity. *Advanced Functional Materials*, 2022, 33.
17 Wang J, Fu S, Huang L, et al. Heterojunction Engineering and Ideal Factor Optimization Toward Efficient MINP Perovskite Solar Cells. *Advanced Energy Materials*, 2021, 11.
18 Huang W, Zhang H, Tang J, et al. Self-Powered Optoelectronic Synaptic Devices for Neuromorphic Computing with the Lowest Energy Consumption Density. *ACS Photonics*, 2024, 11: 3095-3104.
19 Zhang Z, Wang S, Liu C, et al. All-in-one two-dimensional retinomorphic hardware device for motion detection and recognition. *Nat Nanotechnol*, 2022, 17: 27-32.
20 Liu C, Jiang Y, Shen B, et al. A full-featured 2D flash chip enabled by system integration. *Nature*, 2025, 646: 1081-1088.